REPORT DOCUMENTATION PAGE

Form Approved OMB No. 0704-0188

Public reporting burden for this collection of information is estimated to average 1 hour per response, including the time for reviewing instructions, searching existing data sources, gathering and maintaining the data needed, and completing and reviewing the collection of information. Send comments regarding this burden estimate or any other aspect of this collection of information, including suggestions for reducing the burden, to Department of Defense, Washington Headquarters Services, Directorate for Information Operations and Reports (0704-0188), 1215 Jefferson Davis Highway, Suite 1204, Arlington, VA 22202-4302. Respondents should be aware that notwithstanding any other provision of law, no person shall be subject to any penalty for failing to comply with a collection of information if it does not display a currently valid OMB control number.
PLEASE DO NOT RETURN YOUR FORM TO THE ABOVE ADDRESS.

1. REPORT DATE *(DD-MM-YYYY)*
21-05-2003

2. REPORT TYPE
Final Report

3. DATES COVERED *(From – To)*
9 May 2002 - 21-Oct-03

4. TITLE AND SUBTITLE
Coaxial-type resistive sensor for HPM applications

5a. CONTRACT NUMBER
F61775-02-WE030

5b. GRANT NUMBER

5c. PROGRAM ELEMENT NUMBER

6. AUTHOR(S)
Dr. Zilvinas Kancleris

5d. PROJECT NUMBER

5d. TASK NUMBER

5e. WORK UNIT NUMBER

7. PERFORMING ORGANIZATION NAME(S) AND ADDRESS(ES)
Semiconductor Physics Institute
Microwave Laboratory
A. Gostauto 11
Vilnius 2600
Lithuania

8. PERFORMING ORGANIZATION REPORT NUMBER
N/A

9. SPONSORING/MONITORING AGENCY NAME(S) AND ADDRESS(ES)
EOARD
PSC 802 BOX 14
FPO 09499-0014

10. SPONSOR/MONITOR'S ACRONYM(S)

11. SPONSOR/MONITOR'S REPORT NUMBER(S)
SPC 02-4030

12. DISTRIBUTION/AVAILABILITY STATEMENT
Approved for public release; distribution is unlimited.

13. SUPPLEMENTARY NOTES

14. ABSTRACT

This report results from a contract tasking Semiconductor Physics Institute as follows: The contractor will investigate resistive sensors for measuring high power microwave pulses. At the end of this investigation, the contractor will develop a prototype unit of the coaxial-type resistive sensor and test it in a wide frequency and power range.

20040210 118

15. SUBJECT TERMS
EOARD, High Power Microwaves, High Power Microwave Sensors

16. SECURITY CLASSIFICATION OF:			17. LIMITATION OF ABSTRACT	18. NUMBER OF PAGES	19a. NAME OF RESPONSIBLE PERSON
a. REPORT	b. ABSTRACT	c. THIS PAGE			MICHAEL KJ MILLIGAN, Lt Col, USAF
UNCLAS	UNCLAS	UNCLAS	UL	30	19b. TELEPHONE NUMBER *(Include area code)* +44 (0)20 7514 4955

COAXIAL-TYPE RESISTIVE SENSOR FOR HPM APPLICATIONS

(Final report)

DISTRIBUTION STATEMENT A
Approved for Public Release
Distribution Unlimited

Microwave Laboratory, Semiconductor Physics Institute
A.Gostauto 11, Vilnius 2600, Lithuania
tel.: 370 5 261 9808
fax.: 370 5 262 7123
e-mail: kancleris@uj.pfi.lt

Vilnius, 2003

Contents

Contents 2
1 Introduction 3
2 Coaxial-type resistive sensor 4
2.1. The concept 4
2.2. Sensing element 5
2.3. Matching with transmission line 7
2.4. Low-pass filter 7
2.5. Output signal measurement and calibration 8
3 Theoretical consideration of other possible versions of SE 9
4 Realizations of the coaxial-type resistive sensors 10
4.1. Lumped element filter 11
4.2. Hybrid filter 11
4.3. Microstrip filter 12
5 CRS characteristics 13
5.1. Reflection coefficient 13
5.2. Output signal 15
5.3. Time response 19
5.4. Sensor's heating 19
6 Conclusions 20
7 References 21
8 Acknowledgements 21
9 Appendixes 22
9.1. Desirable Technical Specifications 22
9.2. Short description of the FDTD program 22

1 Introduction

Although pulse power of the microwave sources being researched in laboratories, as well as being manufactured by industry, is continuously growing up the methods practically used for pulse power measurement are not adapted for the measurement of high power microwave (HPM) pulses. At present the measurement of the output power of pulsed microwave sources is based on two methods [1].

The first method relies on the measurement of the average power using average power meter. To get the pulse power the measurement result is divided by the duty cycle that is measured with video detector and an oscilloscope. Such technique can be applied for the measurement of HPM pulses. At least two disadvantages of this technique can be mentioned. First, the accuracy of the measurement becomes poor, when applying the method for the measurement of non-rectangular pulses. Second, this technique is of little use when measuring single or low repetition rate pulses.

The other method is based on the conversion of a microwave pulse to the DC pulse using calibrated planar-doped barrier diode. It can be employed for the measurement of HPM pulses as well. Main disadvantage of the diodes when using them for HPM applications is that the diodes can handle only a very low power level. Highest pulse power can be measured by the planar-doped barrier diodes is of the order of 100-200 mW [1]. Therefore, when the diode is applied for the measurement of HPM pulses the initial pulse has to be strongly attenuated. From the one hand, large attenuation of the microwave power results in a decrease in measurement accuracy. In addition, the size and weight of the measurement system increases, its control becomes complicated. From the other hand, when measuring pulsed microwave power of the order of mW, the diode outputs a DC pulse with amplitude of the order of mV. To measure such small DC signal in the presence of stray pick-up and electromagnetic interference that are typical to the environment of HPM sources shielded chambers with the measurement equipment situated at a respectful distance from HPM source are usually employed. Installation of shielded chambers confines the flexibility of the measurement system its price increases.

Having in mind that at present, different types of pulsed high power microwave (HPM) oscillators and amplifiers are used in communication systems, radars, electromagnetic testing facilities, scientific research, and military projects. Many HPM systems should be continuously monitored for output pulse's power level during manufacturing and operation. The large number of measurements involved and their importance dictate that the measurement equipment and techniques should be accurate, reproducible, and convenient to use.

In Microwave laboratory we have developed an alternative device for HPM pulse measurement – resistive sensor (RS) the performance of which is based on electron heating effect in semiconductors. Due to electron heating in the electric field of the microwave pulse the resistance of the RS increases and by measuring this resistance change the microwave pulse power in the waveguide is determined. Main advantages of the RS over the diode are the following: it can measure about 60 dB higher power level, produces high output signal, is overload resistant and demonstrates very good long term stability. The waveguide-type RS developed in our laboratory is used in Russian, Swedish and USA microwave centers. Our activities in a waveguide-type RS area have been described in a recent review article [2].

Unfortunately, waveguide-type RS is not free from some drawbacks. First, the frequency range where the particular device can be used is restricted by the bandwidth of the certain waveguide. Hence for the HPM pulse measurement in a wide frequency range a set of sensors has to be used. Therefore, the measurement system becomes complicated and its cost

increases. Moreover, at a lower frequency size and weight of the waveguide section with the RS increases and it becomes inconvenient in use. Second, as it was shown in [3] the sensitivity of the X-band RS changes more than two times in the frequency band. Likely, that the same frequency response is characteristic to the RS for other frequency bands. These two features of the waveguide-type RS confine its wider application for HPM pulse measurement in a different frequency bands.

Our investigation described in this report is devoted to the development of a coaxial-type RS (CRS). The CRS should keep up the main advantages of the waveguide-type RS (measurement of HPM pulse directly, high output signal), while keeping the other principal characteristics (flatness of frequency response and VSWR) at the same level as of a conventional diode (see Appendix). The final report is organized as follows. In Section 2 the principle of the CRS design is described. In the subsections of this section the concept of the CRS, the sensing element, matching of it with the transmission line, low-pass filter and output signal measurement circuit are considered. The possibilities to consider other possible versions of the SE is discussed in Section 3. Present realizations of the CRS is described in Section 4. Measured CRS characteristics are collected in Section 5. Conclusions, references and acknowledgements are found in Sections 6 to 8. In the Appendixes 9 the desirable technical characteristics and short description of the FDTD program used for calculations are presented. Throughout the report, we used the term "pulse power" to mean instantaneous or envelope power.

2 Coaxial-type resistive sensor

In this section the principle of the CRS design is presented. Main parts of the CRS such as sensing element, matching of the sensing element with the coaxial line, low-pass filter and signal measurement circuit are considered.

2.1. The concept

The CRS is thought to be a two terminal device. One of them will be used to connect the sensor to a coaxial line where the measuring microwave pulse is propagating. The other one is devoted to connect the CRS to the measuring circuit and sensor feeding unit. Two

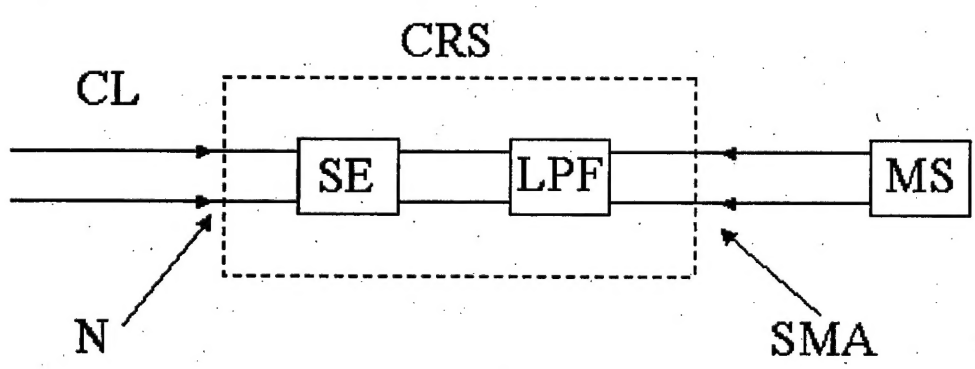

Figure 1. Schematic block diagram of the coaxial-type RS: SE – sensing element, LPF – low-pass filter, CL – coaxial line, N – N-type connector, SMA – SMA-type connector, MS – sensor's feeding and measuring system.

terminal design is typical to the microwave diodes produced by industry except that the diode does not need any feeding system.

We used 50 Ω impedance coaxial line as a basis for the CRS design because waveguide to coaxial line adapters are usually fitted to 50 Ω impedance lines. Therefore, it should not be a problem to connect the CRS to the different band waveguides making use of standard adapters produced by industry.

A sensing element (SE) of the RS "feels" electric field strength of the microwave pulse at the point of the transmission line where it is placed. Therefore, to get correct result when measuring microwave power using such SE the distribution of the electric field amplitude in the transmission line should be homogeneous or the reflection of the microwaves from the SE as well as from the end of transmission line should be negligible. To fulfill these conditions for the waveguide-type RS the SE with small reflection coefficient is designed and the matched load is attached to the end of the waveguide. Application such concept of design to the CRS faces with some difficulties. Therefore, after some experimental investigation that was performed earlier and described in the interim report [4], it was decided to skip the matched load and the SE should serve not only as the sensor detecting microwave pulse power but as a matched load as well.

Schematic block diagram of the proposed version of the CRS is shown in Figure 1. It is seen that CRS actually consists of the SE and low-pass filter. One contact of the SE is directly connected to the coaxial line's conductor, while the other one – to the coaxial line's shielding. Therefore the SE serves as a matched load and a pulse power detector simultaneously. To achieve good matching of the CRS with the coaxial line the resistance of the SE is set to be 50 Ohms. Since the dimensions of the sensing element are chosen much less than the wavelength of the microwave, the SE might be considered as a lumped element of the circuit. This is a main reason why a good matching might be achieved in a wide frequency range [4].

The main purpose of the low-pass filter of the CRS is to prevent the direct propagation of the microwave pulse to the measuring unit. At the same time the low-pass filter should not spoil the matching of the SE with the coaxial line in a wide frequency band. And finally, the parameters of the low-pass filter influences on the response time of CRS. Therefore all three factors have to be taken into account when choosing parameters of the low-pass filter.

The coaxial line to the CRS is attached via N-type connector, while for the connection of the CRS to the measuring circuit and feeding unit SMA-type connector is used. DC pulse supply without amplification [2] as well as DC feeding with a DC pulse amplifier can be attached to the CRS. Depending on the requirements of the customer amplifier and DC source can be integrated into CRS.

Summarizing it has to be pointed out that a new concept of the RS design has been used in the CRS construction. The sensing element of the CRS is directly connected to the coaxial line's conductor therefore it simultaneously operates as a microwave pulse power measuring unit and a matched load of the coaxial line.

2.2. Sensing element

Since the resistance change of the semiconductor is the basis for the RS operation, so for pulsed HPM measurement we use a resistor made from n-type Si. The view of the SE is shown in **Figure 2**. It is seen that the sensing element is a cube-shaped piece of Si with Ohmic contacts on its ends. The SE is processed from a wafer of n-Si with specific resistance $\rho = 5\ \Omega cm$. The thickness of the wafer is chosen 1 mm that corresponds to the height of the sensing element. To form Ohmic contacts the impurity diffusion process is employed that is

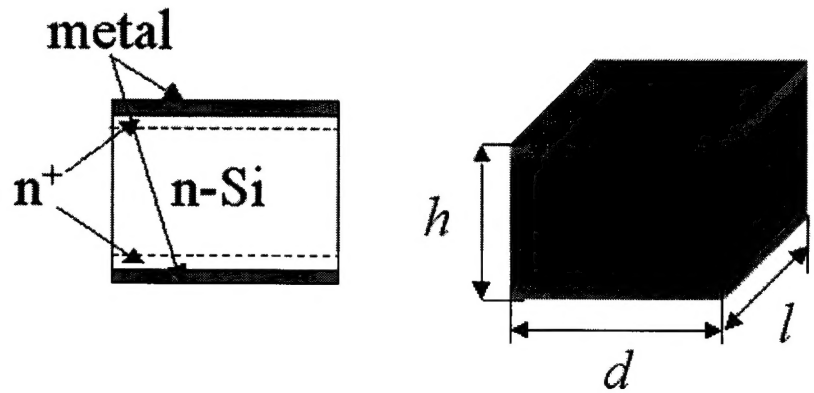

Figure 2. The view of the sensing element of the CRS. The dimensions of the sensing element are the following h=1 mm, $d \approx l \approx 1$ mm, specific resistance ρ=5 Ωcm. Width d and length l of the SE is adjusted individually for each SE to get its resistance 50 Ω.

followed by metal evaporation. Cube-shaped pieces are cut from the wafer. Since the specific resistance varies within the wafer, the cross-section dimensions have been chosen larger than 1x1 mm^2. To get the final resistance of the SE 50 Ω the dimensions of each sensor have been adjusted individually. Therefore the dimensions of the SE are roughly 1x1x1 mm^3. Comparing the dimensions of the SE with microwave wave length in a frequency range 2-10 GHz (15-3 cm) it is seen that the dimensions of the SE is much less than the wave length and it might be considered as a lumped element in all frequency range under consideration.

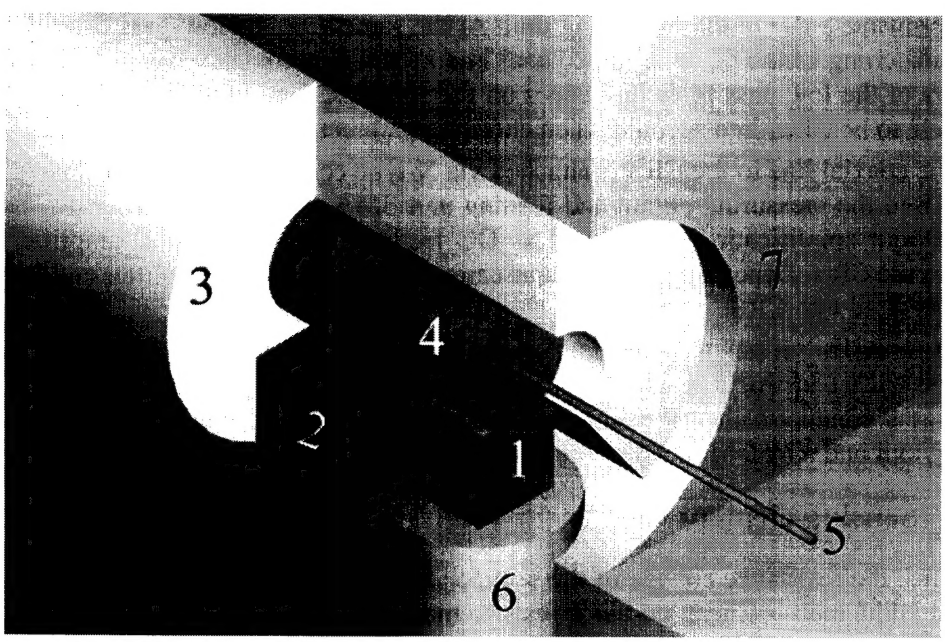

Figure 3. The sketch of the connection of the SE with the coaxial line, 1 – SE, 2 – ceramics (ε=10) insert for SE matching, 3 – coaxial line's insulator (Teflon), 4 – inner conductor of coaxial line, 5 – thin metal wire for filter connection, 6 – piston for SE mounting, 7 – metal body.

2.3. Matching with transmission line

The drawing of the connection of the SE with coaxial line is shown in **Figure 3**. As one can see from the figure the sensing element is mounted between the gilded moving piston and inner conductor of the coaxial line. The piston is pressed by the metal spring and it assures good mechanical and electrical contacts. The matching of the SE with coaxial line is achieved by changing the width of ceramics (ε=10) insert. The rest part of the coaxial line between inner and outer conductors is filled with Teflon. The end of the inner conductor of the coaxial line coincides with the ends of the sensing element. Small diameter hole was drilled in the inner conductor and thin wire was soldered into it. The wire is used to connect the low-pass filter. Such a construction of the connection of the SE to the coaxial line without the wire provides VSWR less than 1.25 in a frequency range 2-12 GHz.

2.4. Low-pass filter

Buterworth and Chebyshev filters consisted of different number of elements have been considered in the interim report [4]. Finally five elements Butterworth filter has been selected. Main arguments favored for this type of filter were the following: (1) sufficiently high roughly 60 dB attenuation of the signal is achieved at $3f_c$ where f_c is a critical frequency of the filter, (2) flat transfer function in the band-pass, (3) shorter response time.

The equivalent circuit of employed filter is shown in **Figure 4**. The expressions those allow to determine the magnitudes of the inductances and capacitances that comprise five elements Butterworth filter can be found in any textbook on microwave circuits [5] and are collected in Table 1. Using them the parameters of the filters for different critical frequencies have been calculated. As it was described in the interim report [4] three different types of filters were used in the CRS. They are lumped element filter, hybrid filter and distributed element filter made from the sections of microstrip line. Particular filters in more detail are

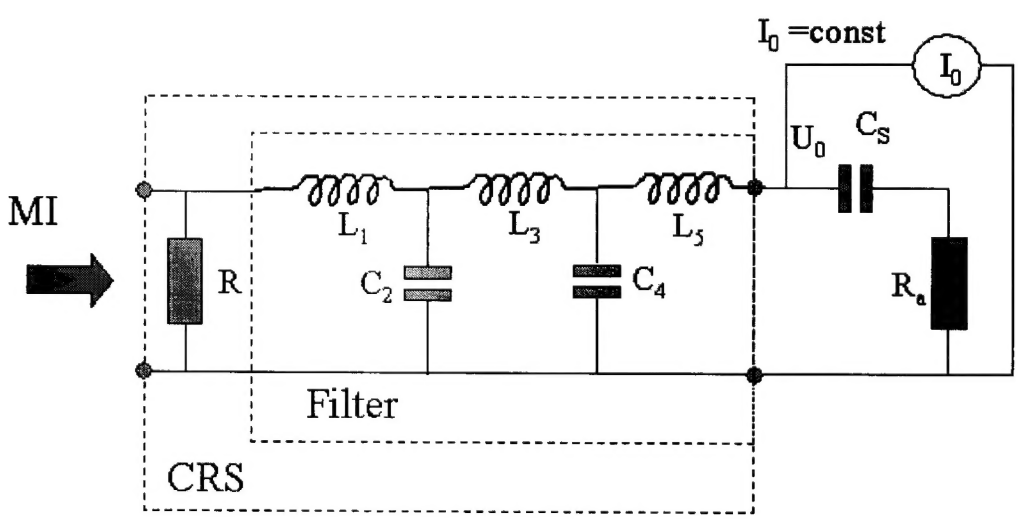

Figure 4. Equivalent circuit of the CRS with 5 elements low-pass filter fed by the constant current I_0 from current source. L_1, L_3, L_5 are the inductances and C_2, C_4 – capacitances of the filter, R is the resistance of the SE, U_0 is voltage drop on it in the absence of microwave pulse, C_s is a separating capacitor, R_a is an input resistance of the oscilloscope, MI denotes microwave input.

described in Section 4.

Table 1. g-parameters of 5 element Butterworth type filter and formulas to calculate the inductances and the capacitances of the elements of the filter [5].

No of element	g-parameter	Expression
1 & 5	0.618	$L_1 = L_5 = \frac{g_1 \cdot R_a}{2\pi f_c}$
2 & 4	1.618	$C_2 = C_4 = \frac{g_2}{2\pi f_c \cdot R_a}$
3	2.000	$L_3 = \frac{g_3 \cdot R_a}{2\pi f_c}$

2.5. Output signal measurement and calibration

Equivalent circuit that is used for the feeding of the RS and the output signal measurement is shown in **Figure 4**. Constant current source is used to feed the CRS. In the absence of the microwave pulse the voltage fall on the SE is $U_0=I_0R$ where R is the resistance of the SE in the absence of microwave pulse and I_0 is the amplitude of the current. Before the microwave pulse is triggered the capacitors C_2, C_4 and C_s are charged up to a voltage U_0, and DC current flows only through the arm of the circuit with the SE. Microwave electric field induces the resistance change of the sensor and the current flowing through it should decrease. Since the current from the DC source is kept constant, the current flowing in the other arm of the circuit should increase by the same amount. Denoting this current change as ΔI and taking into account that the change of the voltage must be equal in both arms of the circuit the following relation can be readily written down

$$I_0 \cdot \Delta R - \Delta I \cdot R - \Delta I \cdot \Delta R = \Delta I \cdot R_a, \tag{1}$$

where ΔR is the resistance change of the sensor due to electron heating and R_a is the input resistance of the oscilloscope. From (1) the current change due to sensor's resistance increase can be expressed as

$$\Delta I = \frac{I_0 \cdot \Delta R}{R_a + R + \Delta R}. \tag{2}$$

Since the output signal registered by an oscilloscope is simply $\Delta I \cdot R_a$, the final expression binding the output signal with the relative resistance change of the sensor can be obtained from (2)

$$U_S = U_0 \frac{\frac{\Delta R}{R}}{1 + \frac{R}{R_a}\left(1 + \frac{\Delta R}{R}\right)}. \tag{3}$$

As follows from (3) the largest output signal from the CRS will be obtained when $R \ll R_a$. The resistance of SE cannot be decreased, since it should be matched with the impedance of the coaxial line (50 Ω). The only way to raise the amplitude of the output signal is to use high input resistance of the oscilloscope. Although this should increase the response time of the CRS but for the sensor calibration we are using sufficiently long microwave pulse (>1μs) and a short connection cable. Therefore, even using high input resistance of the oscilloscope the response time of the CRS is short enough to measure the amplitude of such pulse. In the limit $R \ll R_a$ the output signal is proportional to the relative resistance change of the SE

$$U_S = U_0 \frac{\Delta R}{R}. \tag{4}$$

When the CRS is calibrated the dependence of U_S versus microwave pulse power P is measured and a set of pair of numbers is determined

$$P_i, U_{Si} \quad i = 1, 2, \ldots N \tag{5}$$

Making use of (4) the relative resistance can be expressed as a function of the output signal

$$\frac{\Delta R}{R} = \frac{U_S}{U_0}, \tag{6}$$

and instead of (5) a set of pairs of

$$P_i, \frac{\Delta R_i}{R} \quad i = 1, 2, \ldots N \tag{7}$$

can be determined. It was shown in [2] that quadratic polynomial fits well the dependence of P on the relative resistance change, therefore, that dependence can be written down in the following way

$$P = A \cdot \frac{\Delta R}{R} + B \left(\frac{\Delta R}{R} \right)^2 \tag{8}$$

Fitting experimental data (7) by (8) in a least square sense the empirical parameters A and B describing measured experimentally output characteristic of the sensor is determined. Inserting (6) into (8) we arrive to the final expression that describes the dependence of pulse power on the output signal

$$P = A \cdot \frac{U_S}{U_0} + B \left(\frac{U_S}{U_0} \right)^2 \tag{9}$$

Summarizing it has to be pointed out that output voltage-power characteristic is measured for each CRS at different frequencies. The parameters A and B are determined from the measured dependencies of the output signal on the input pulse power. Using (9) the pulse power can be easily calculated from the measured signal U_S. The parameters A and B determined for the particular CRS at different frequencies can be employed to analyze the dependence of output signal on frequency in a low signal and large signal limits. It should be noted that high amplitude (50 V) DC pulse synchronized with the measuring pulse could also be used with the CRS and it allows increasing the output signal of it [4].

3 Other possible versions of SE design

To consider other possible versions of the construction of the SE theoretically we have developed a program that solves Maxwell's equations numerically using FDTD (finite different time domain) method [6]. The program calculates distribution of electric and magnetic fields in the coaxial line with the semiconductor insert placed in it. It allows to calculate the reflection coefficient from the semiconductor obstacle and the average electric field strength in it. Short description of the program is presented in the Appendix Section 9.2. The program has been finished just before the end of this contract and we were enable to perform consistent calculations of the distribution of the electric field in the semiconductor obstacle that partly fills the cross section of the coaxial line. We hope to perform them in a nearest future

4 Realizations of the coaxial-type resistive sensors

In this section the photos of the CRS with different type of low-pass filters are presented. The lumped element, hybrid and microstrip filters realizations are shown.

The general view of the CRS is shown in **Figure 5**. It is seen that the SE and low-pass filter are placed in the parallelepiped shaped metal box closed with the metal cover that is fixed with four screws. The total length of the device including the lengths of N-type and SMA connectors is roughly 10 cm, the width 2.5 cm, and the height – 2 cm.

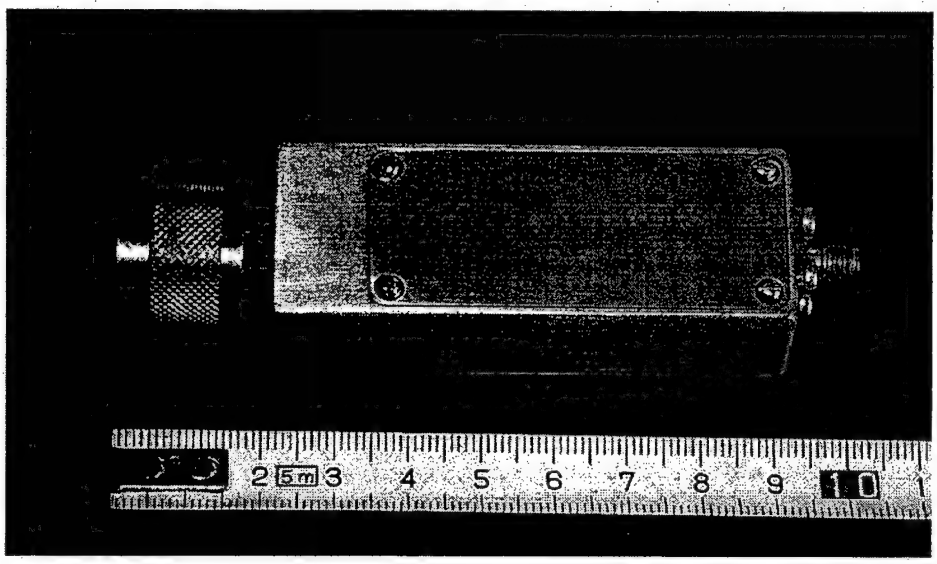

Figure 5. General view of the CRS.

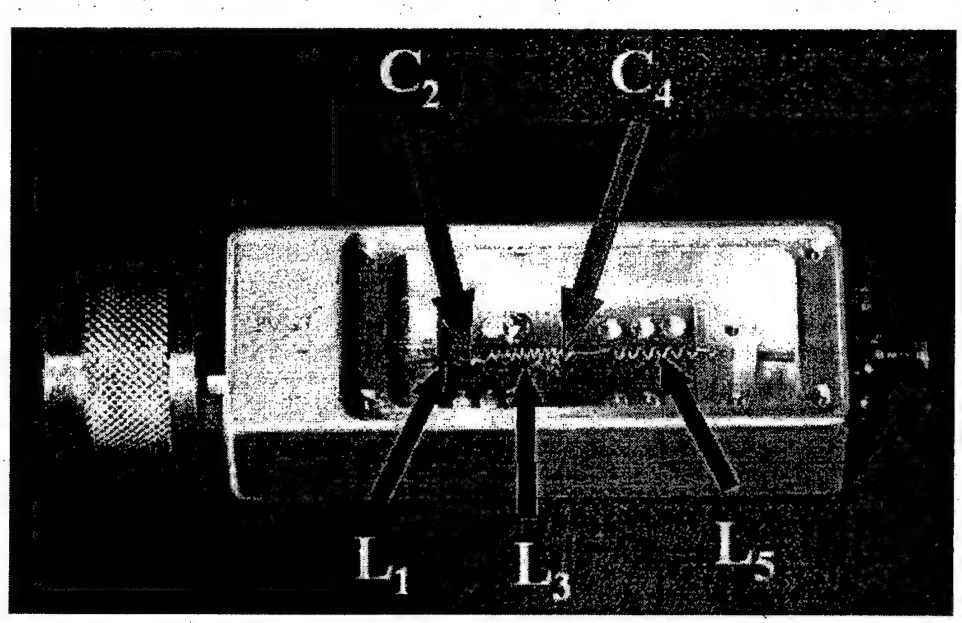

Figure 6. A view of the CRS with lumped element filter. L_1-L_5 and C_2, C_4 the inductances and the capacitors of the filter are indicated.

4.1. Lumped element filter

The view of the CRS with lumped element low-pass filter is shown in **Figure 6**. The lumped elements of the filter capacitors and inductances are marked in the figure by letters C and L, respectively. As the elements of lumped element filter the home made inductances and high frequency capacitors were used. The inductance is a coil twisted from thin wire (∅0.1 mm). The diameter of the coil was roughly 1.5 mm. The diameter of the coil, number of turns and coil pitch have been calculated using well known formula binding those parameters with coil inductance. The critical frequency of lumped element low-pass filter was chosen f_c=0.75 GHz. The capacitance and inductance of filter elements were determined making use formulas presented in Table 1.

4.2. Hybrid filter

The view of the CRS with hybrid filter is shown **Figure 7**. As in the case of lumped element filter the hybrid filter elements are home made inductances and high frequency capacitors except the first inductance. Since it has the largest influence on the filter performance in a high frequency region, the first inductance is partly accomplished as conductor coated by the layer of ferrite and partly as a lumped element inductance. A small diameter hole is drilled in the ferrite plate and a wire is passed through it. As in the case of lumped element low-pass filter the inductances were accomplished as a coils twisted from thin metal wire (∅ 0.1 mm). The ferrite, capacitors and lumped inductances are marked in the figure by letters F, C and L. Including the ferrite in the low-pass filter we were able to improve its performance in high frequency region and, as will be shown in the next chapter, the CRS with such type of the filter can be used in the widest frequency range. The critical frequency of lumped element low-pass filter was chosen f_c=0.5 GHz. The capacitance and inductance of filter elements were determined making use formulas presented in Table 1.

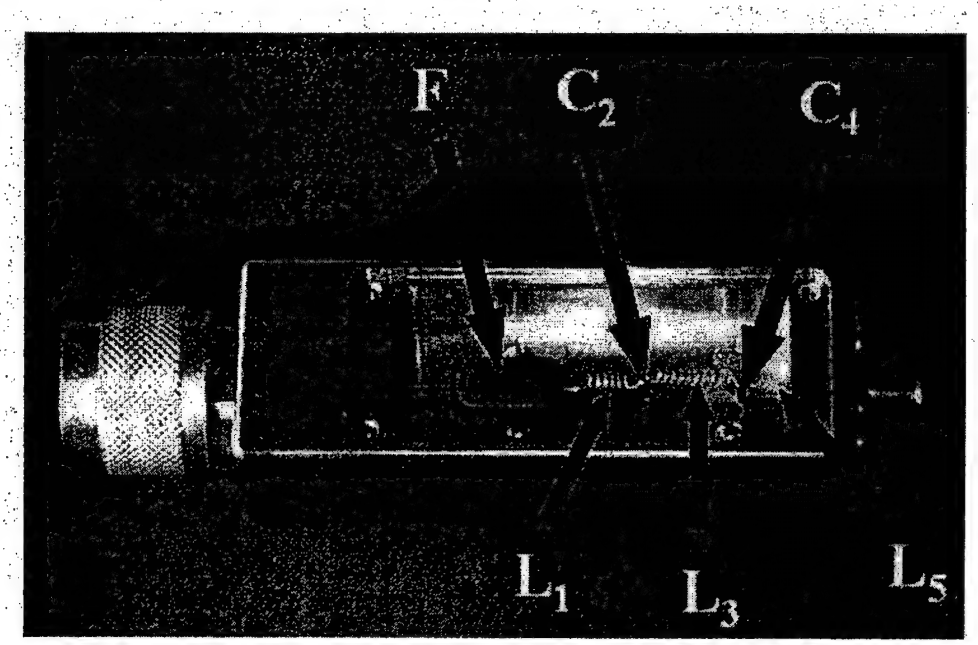

Figure 7. A view of the CRS with hybrid filter. L_1-L_5 and C_2, C_4 the inductances and the capacitors of the filter are indicated. F is a piece of ferrite.

4.3. Microstrip filter

Microstrip filter is composed of the distributed elements corresponding to the lumped elements – inductances and capacitors in prototype filter. The capacitance and inductance of the elements of prototype filter were determined making use formulas presented in Table 1. The segments of different impedance microstrip lines were used to create the corresponding element of the filter. Large impedance (125 Ω) sections correspond to the inductances, while low impedance (20 Ω) sections comprise the capacitors. The view of the CRS with microstrip filter is shown in **Figure 8**. As in the previous figures letters C and L marked the segments of microstrip line corresponding to capacitors and inductances respectively. M denotes the 50 Ω impedance microstrip line connecting the end of the filter to the SMA connector that is devoted to attach the measuring circuit and sensor feeding unit to the CRS. The critical frequency of the microstrip filter is chosen f_c=2.75 GHz allowing to use the CRS in higher frequency range 4-12 GHz. The microstrip lines have been fabricated on 1.5 mm thickness glass laminate substrate (ε=5.5). The width and length of corresponding segments of the microstrip lines were calculated using well known formulas that can be found any textbook on microwave circuits (see for example [5]).

When the metal box with low-pass filter inside has been closed with the metal cover some resonance pikes were found in the frequency range 7-12 GHz. To avoid such resonance that may appear at a frequency where the characteristic dimension of the box becomes multiple to the half wavelength of microwaves, the pieces of absorber were stuck up to the inner side of the metal cover. The view of the metal cover with the pieces of absorber is shown in **Figure 9**. The height of the pieces of absorber was roughly 5 mm. Making use of absorbers eliminate the resonance and improves CRS characteristics in a high frequency region.

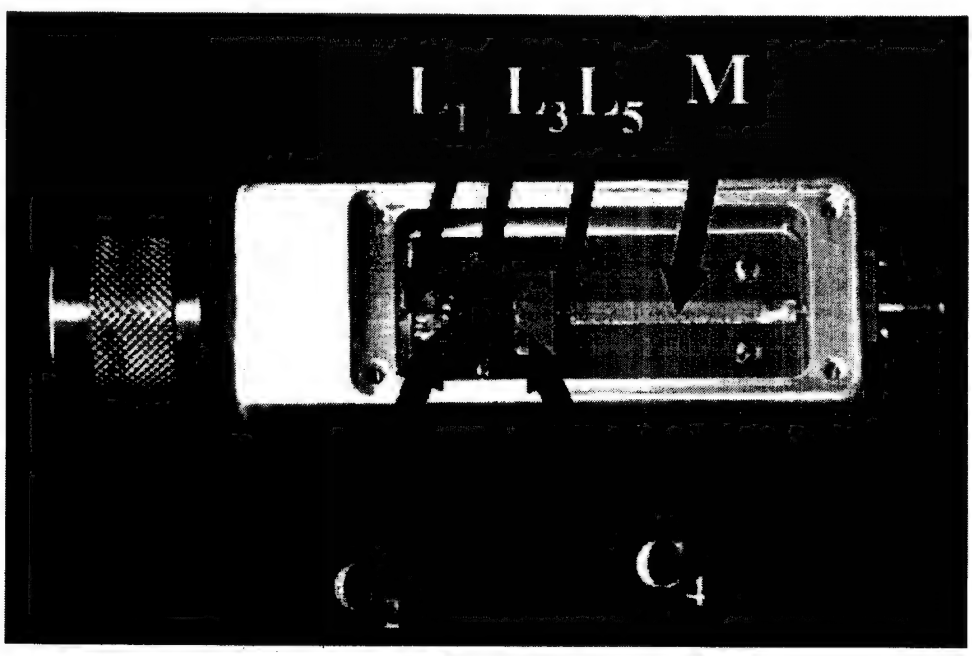

Figure 8. A view of the CRS with distributed element filter. L_1-L_5 and C_2, C_4 the inductances and the capacitors of the filter are indicated. M is the 50 Ω impedance microstrip line.

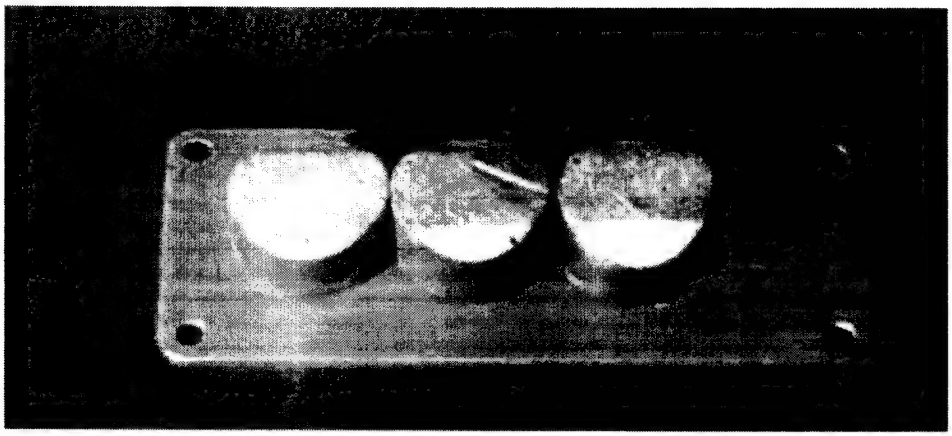

Figure 9. A metal cover of the CRS with the pieces of absorbers mounted on the inner side of it.

5 CRS characteristics

A few CRS with each type of low-pass filter has been manufactured and tested. In this section measurement results are collected. Reflection coefficient, output signal, time response and SE heating investigation results are presented in this section.

5.1. Reflection coefficient

Measurement results of reflection coefficient of the manufactured CRS with different type of filters described in previous section are collected in **Figure 10**. Five elements Butterworth filter was manufactured. The reflection coefficient has been measured in a frequency range 1.25-12 GHz. In the desirable technical specifications that are given in the Appendix the required voltage standing wave ratio (VSWR) of the CRS should be less than 1.6. It corresponds to the reflection coefficient Γ=0.23. This desirable reflection coefficient level is denoted in the figure by a solid line.

The reflection coefficient dependence on frequency for the CRS with lumped element filter (f_c=0.75 GHz) is shown in **Figure 10**(a). It is seen that in the frequency range 1.25-6 GHz the CRS with lumped element filter exhibits sufficiently low reflection coefficient values that meets the requirements of the desirable technical specifications. At a higher frequency the electrical length of the lumped elements becomes too large in comparison with the microwave's wavelength and this is the reason why some resonance may occur and the peaks are seen in $\Gamma(f)$ dependence.

It seems that the largest influence to the resonance that appears at higher frequency should have the first inductance of the filter that is directly connected to the SE. Therefore, before the first inductance the section of the transmission line is inserted that is made using the conductor coated by a layer of ferrite. The transmission line is made of the plate of the ferrite (50ВЧ) in which the small diameter hole has been drilled and a metal wire is passed through it. Measured reflection coefficient dependencies on frequency for such type of filter (f_c=0. 5 GHz) are shown in **Figure 10**(b). It is seen that insertion of the additional transmission line improves performance of the filter in a high frequency region. It should be noted that some increase of the reflection coefficient is registered in a low frequency range 1.25-2 GHz in comparison with the CRS with lumped element filter but reflection coefficient in this region does not exceed the value indicated in the desirable technical specifications.

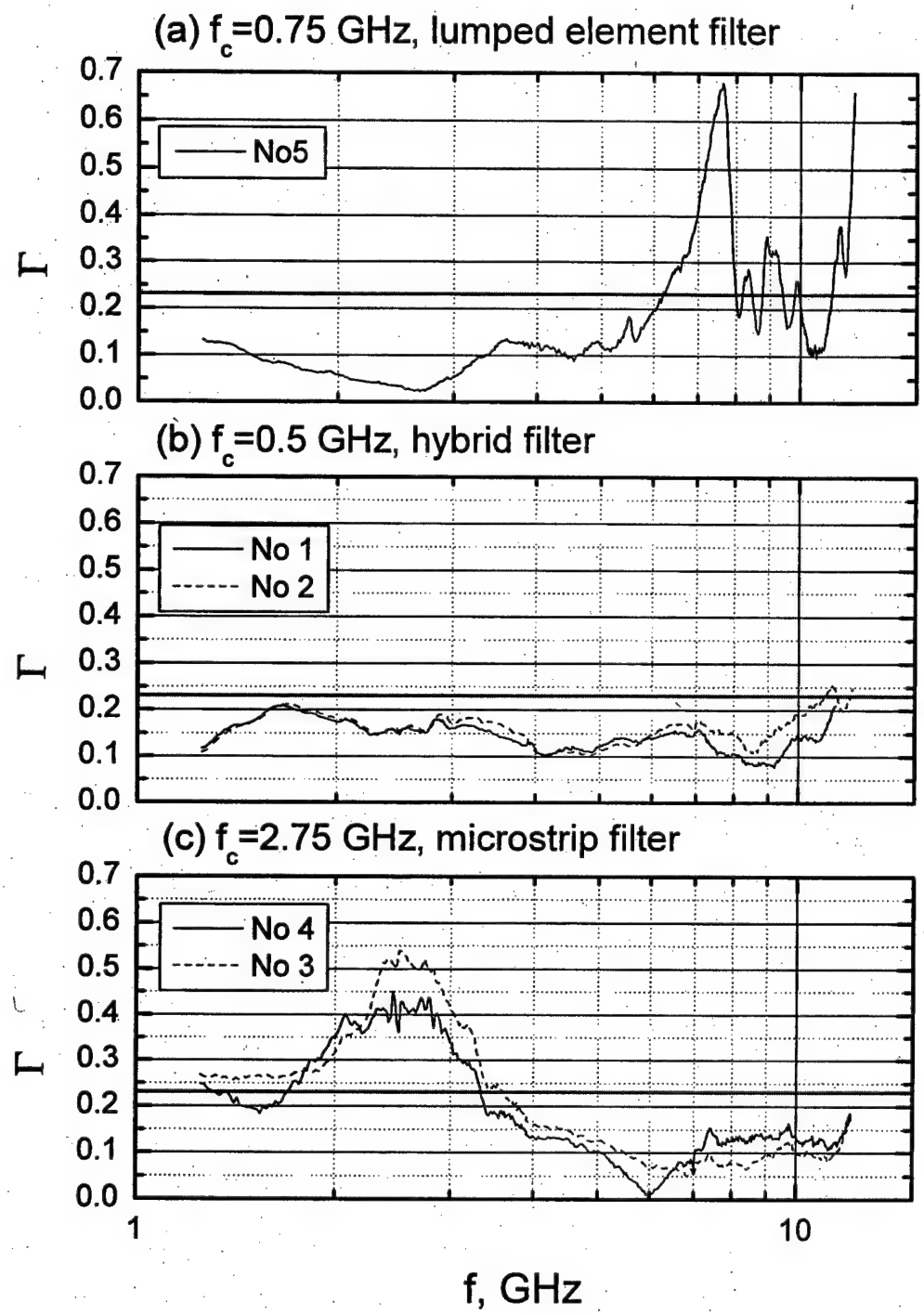

Figure 10. Measured dependencies of reflection coefficient for the CRS with different realizations of 5 elements Butterworth filter: (a) lumped element filter f_c=0.75 GHz, (b) lumped element filter with additional ferrite line as a part of the first inductance of the filter f_c=0.5 GHz, (c) distributed element filter made of the segments of different impedance microstrip line. Solid line in the figure denotes the highest limit of the reflection coefficient allowed by desirable technical specification presented in the Appendix.

Therefore, the CRS with hybrid type low-pass filter practically fulfill requirements for the value of the reflection coefficient in whole frequency range under consideration.

The results of the measurement of the reflection coefficient for the microstrip filter with critical frequency f_c=2.75 GHz is shown in **Figure 10**(c). It is seen that in the frequency range 4-12 GHz the CRS with distributed element filter exhibits sufficiently low reflection coefficient values that meets the requirements of the desirable technical specifications.

5.2. Output signal

Three powerful microwave generators that can produce over 1 kW pulse power at a fixed frequency in S (f=2.75 GHz), C (f=5.7 GHz) and X (f=9.3 GHz) bands are in operation in the Microwave laboratory. Therefore, the output signal dependencies on microwave power might be measured at those frequencies up to a maximum pulse power 1 kW. Output signal for particular device is not measured at frequency for which the reflection coefficient value does not meet the requirements of desirable technical specifications. Therefore, the CRS with hybrid filter is measured at all frequency bands, the CRS with lumped element filter is tested at S and C whereas the CRS with microstrip filter – at C and X bands.

The experimental setup for CRS calibration is shown in **Figure 11**. The CRS under investigation is connected to the waveguide via waveguide to coaxial adapter. Reference waveguide-type RS connected to the main waveguide via directional coupler serves as a reference pulse power meter that maintains a constant pulse power in a main waveguide. Changing the attenuation of the precise variable attenuator the pulse power delivered to the CRS is changed. The CRS is fed using constant current source that produces roughly 80 mA current. The current was adjusted before the measurement of each CRS to get 4 V DC voltage drop on the SE in the absence of microwave pulse. The signals from the CRS and the reference RS are measured using dual-channel oscilloscope Tektronix TDS 520. Prior to measuring output characteristic of the CRS the reading of the reference RS is linked with the absolute power level delivered to the coaxial line via the waveguide to coaxial line adapter.

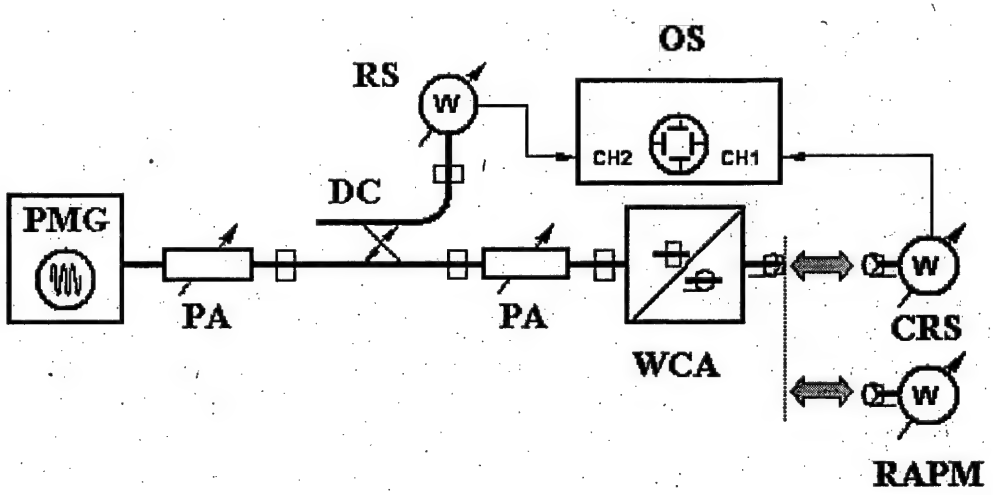

Figure 11. The experimental setup for CRS calibration: PMG: pulse microwave generator, PA: precise variable attenuator, DC: directional coupler, RS: reference resistive sensor, OS: oscilloscope Tektronix TDS 520, WCA: waveguide to coaxial adapter, RAPM: Rohde & Schwarz reference average power meter NRVS with power sensor NRV-Z54, CRS: CRS under test.

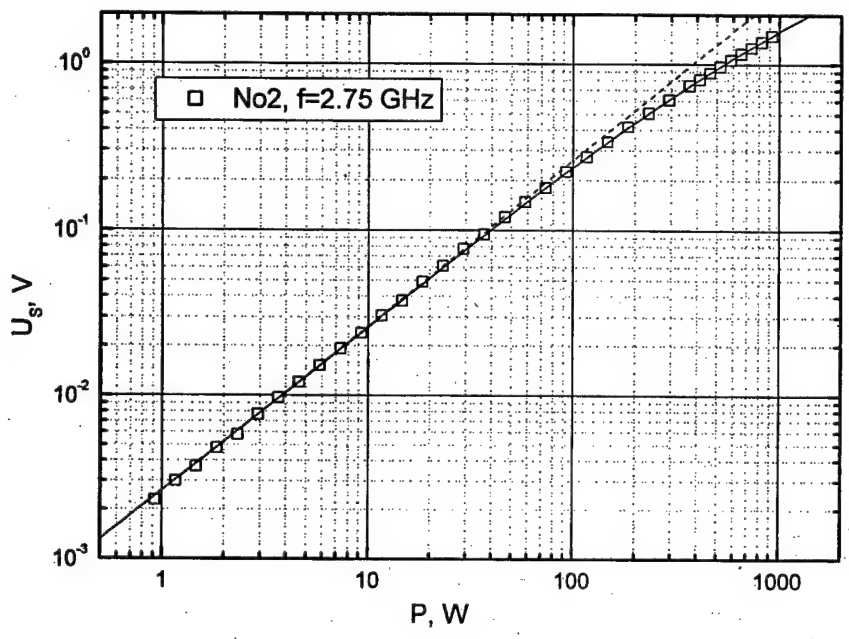

Figure 12. Typical dependence of the output signal of the CRS on microwave pulse power measured making use constant DC current source. DC voltage drop on the SE in the absence of microwave pulse is 4 V. Points denote experimentally measured data for CRS No 2 with hybrid filter at f=2.75 GHz, solid line corresponds to the polynomial approximation (9), dashed line demonstrates linear approximation.

To do that the power sensor NRV-Z54 of the Rohde & Schwarz reference average power meter NRVS is connected to the coaxial to waveguide adapter. Measuring simultaneously the readings of averaged power meter and reference RS the absolute power level delivered to coaxial line is linked with the reading of the reference RS. Therefore, restoring the same reading of the reference RS during measurement procedure the drift of the pulse power generated by the pulse power generator is eliminated.

Typical dependence of the output signal of the CRS on microwave pulse power is shown in **Figure 12**. Solid line in the figure shows quadratic polynomial approximation of the measured data according to the expression (9). It is seen that two-term approximation fits well measurement results. Dashed line in the figure shows linear approximation i.e. the region where the relative resistance change of the SE linearly depends on microwave power. In this region the output characteristic of the sensor is determined by the value of the coefficient A in the expression (9). Therefore, wishing to compare the readings of the CRS at different frequencies we have compared the value of the coefficient A and the maximum value of the output signal at a power of 1 kW U_{Smax}. The values of those parameters for the different CRS determined from the measurement results at different frequencies are collected in Table 2. In the table together with the values of A and maximum output signal at pulse power 1 kW the variation of those parameters over measured frequency range is calculated according to the expression

$$\mathrm{var}\, A = \frac{A_{\max} - A_{\min}}{A_{\max} + A_{\min}}, \tag{10}$$

where A_{max} and A_{min} are the maximum an minimum values of the parameter in the frequency range under consideration. As one can see from the table the scattering of the output signal is

largest for the CRS with hybrid filter but this is not surprising, since these devices have been tested in the widest frequency range. The CRS with lumped element and microstrip filters are tested in narrower frequency range and demonstrate very small variation of the output signal

Table 2.The values of the parameter A and maximum output signal of the different CRS at P=1 kW.

No	S-band f=2.75 GHz		C-band f=5.7 GHz		X-band f=9.3 GHz		var A %	var U_s %
	A	U_{Smax}, V	A	U_{Smax}, V	A	U_{Smax}, V		
1	1601	1.61	1326	1.7	1292	1.79	±11	±5
2	1516	1.58	1275	1.71	1336	1.73	±9	±5
3			1131	1.94	1144	1.88	±0.5	±0.3
4			1189	1.87	1212	1.86	±1	±1
5	1030	2.17	1056	1.95			±1	±5

with frequency. The variation of the output signal between different CRS with same filter at a fixed frequency is also small. Comparing CRS No1 and No2 with hybrid filter it is seen that difference between parameters A and U_{Smax} at particular frequency does not differ more than 4%.

We also perform additional measurements of the frequency response of the CRS in the frequency range 8-12 GHz using TWT that provide pulse power up to 50 W. The experimental setup used for output signal measurement was similar to that is shown in **Figure 11**. Since the available pulse power from the TWT is too low to measure whole output characteristic of the CRS, only the coefficient A that defines output signal characteristic in the region where the relative resistance change of the SE linearly depends on microwave power (8) is determined from experiment results. The values of the coefficient A for the CRS with hybrid, microstrip and lumped element filters are shown in **Figure 13**. In the last case only values of the parameter A measured in S and C bands are shown. As one can see from the figure the frequency dependence of the sensitivity for the CRS with lumped element filter in the frequency range 2.75-5.7 GHz is negligible. For the CRS with microstrip filter in the frequency range 5.7-12 GHz the output signal variation with frequency does not exceed more than ±8 %. The largest variation of the output signal was found for the CRS with hybrid filter. But it worth to mention that this type of the CRS was tested in the widest frequency range 2.75-12 GHz. The coefficient A slightly decreases with frequency in the range 2.75-12 GHz for both tested CRS with hybrid filter. The output signal in the linear region is inversely proportional to the parameter A ($U_s \sim P/A$ (9)). Therefore, the sensitivity of the CRS with hybrid filter, in general, is slightly increasing with frequency.

Summarizing it has to be pointed out that designed and fabricated the prototype units of the coaxial-type RS with hybrid filter meet all requirements of desirable technical specifications. The CRS with other type of filters also demonstrate very small variation of the output signal with frequency but in narrower frequency band. It should be very desirable to test the CRS additionally in the frequency range 3-5 and 6-8 GHz.

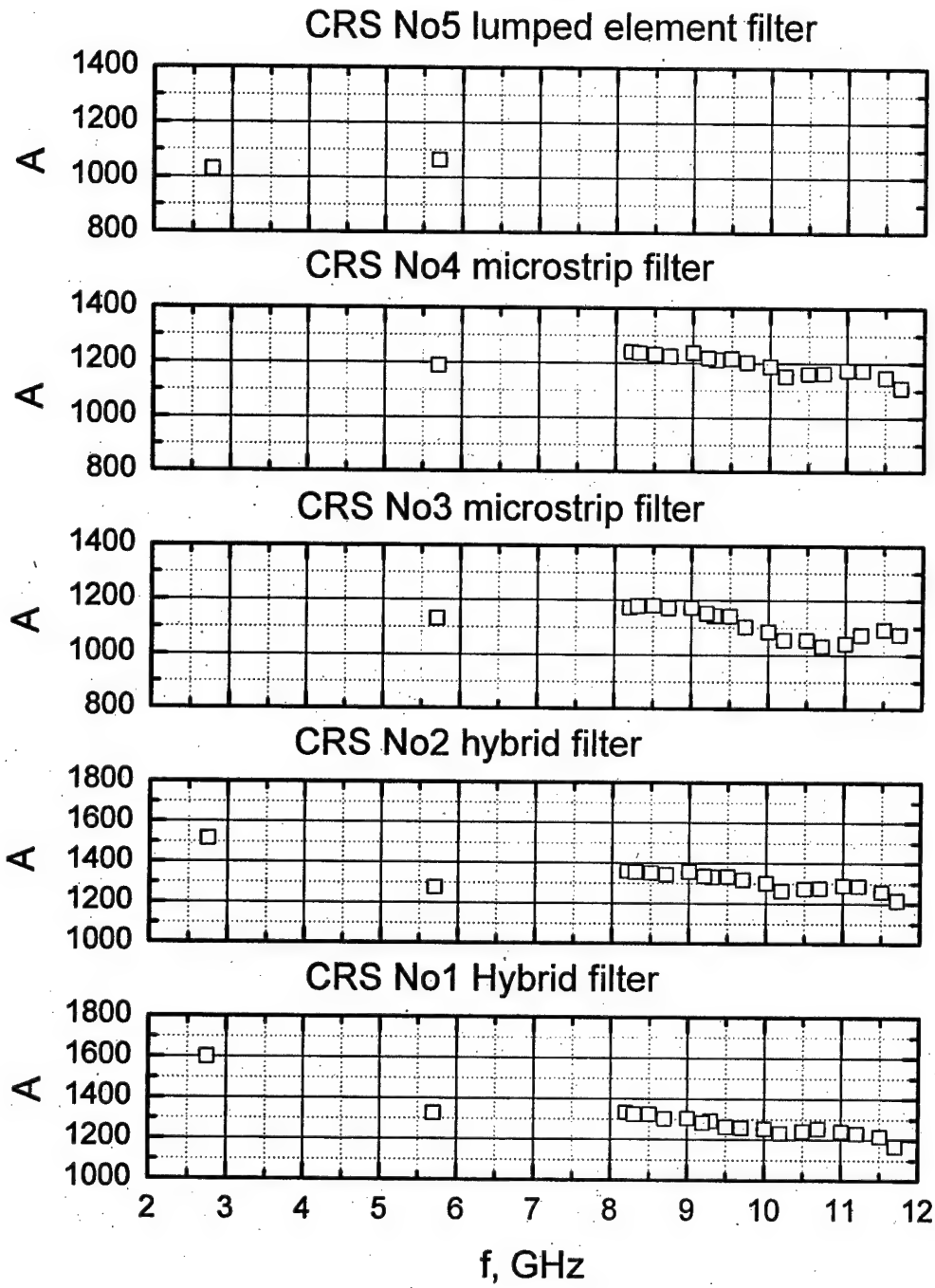

Figure 13. The dependence of the coefficient A on frequency including measurement results using TWT for the CRS with different type of filters.

5.3. Time response

The response time of the SE with different type filters have been tested as well. To do that the DC pulse with subnanosecond rise time is delivered to the input of the CRS and pulse shape in the output is measured. Measurement results for the CRS with three different types of the filters are shown in **Figure 14**. In the figure normalized to the maximum value voltage is presented as a function of the time. It is seen that the both lumped and microstrip filters demonstrate practically identical shape of the DC pulse in the output. Some overshoot is characteristic to these pulses. Estimated from the shape of the measured pulse the response time of the CRS with such filters is roughly $2/f_c$. When the ferrite transmission line is used the shape of the observed pulse is different. The overshoot disappears and the response time is longer $\sim 3/f_c$. The shortest length of the microwave pulse that can be measured by particular device from **Figure 14** can be estimated. It should be more than 20 ns, 10 ns and 5 ns for the CRS with hybrid, lumped element and microstrip filters respectively.

5.4. Sensor's heating

The heating of the sensor during the microwave pulse and average heating when the sequence of microwave pulses is applied to the CRS is analyzed in the interim report [4]. It worthwhile to remind that duration of the pulse is usually much shorter than the heat relaxation time τ_h characterizing the rate of the heat extraction from the sensing element to the environment. Therefore, during microwave pulse heat is practically accumulated in the SE and its temperature increases linearly with time. Using for SE manufacturing n-type silicon with specific resistance 5 Ωcm enables to measure 10 μs duration pulses with 5% pulse distortion. By increasing the specific resistance of the material used for SE manufacturing the

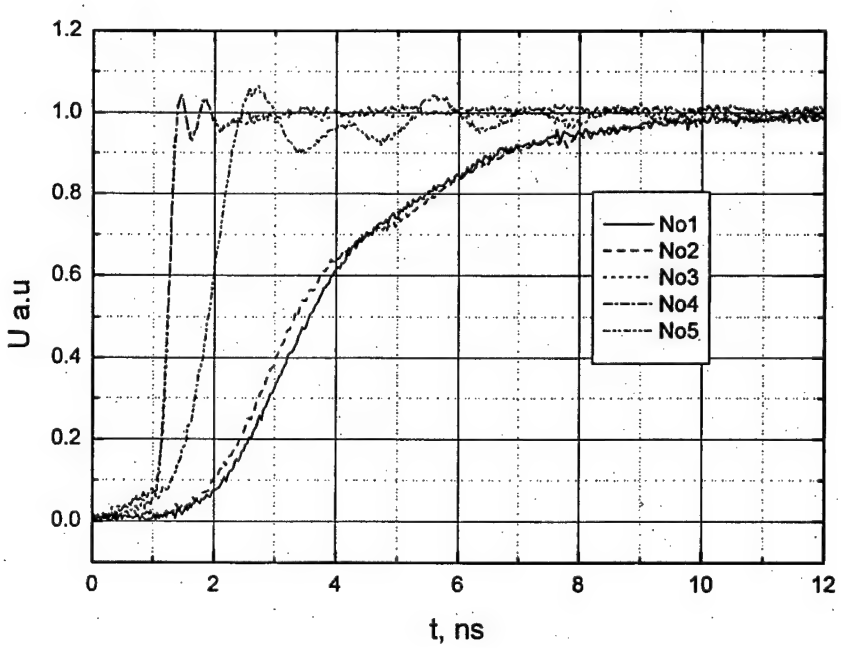

Figure 14. The shapes of the rectangular voltage pulse having passed through CRS with different type filters. No1 and No2: hybrid filter (f_c=0.5 GHz), No3 and No4: microstrip filter (f_c=2.75 GHz) and No5: lumped element filter (f_c=0.75 GHz).

distortion might be decreased.

When the sequence of microwave pulses of duration τ and period τ_0 is applied to the sensor, the average temperature change can be easily obtained from the solution of energy balance equation in the limit $t >> \tau_0, \tau_h$. Averaging temperature change over the period τ_0, one obtains

$$\overline{\Delta T} = \frac{P\tau_h}{Vcd}\frac{\tau}{\tau_0}. \tag{11}$$

Here P is pulse power transmitted to the SE, V is a volume of the SE, c is the specific heat capacity and d is the density of material. All values of parameters appearing in (11) are known except heat relaxation time τ_h. Therefore, by measuring τ_h the average heating of the sensor can be estimated.

To determine the resistance change of the SE due to heating a simple voltage divider scheme is used. The CRS is connected in series with 5 Ω resistor and the voltage drop on it is measured when 200-300 ms duration 10 V amplitude DC pulse is applied to the scheme. Electron heating effect is negligible at such electric field strength ($\Delta R/R \approx 10^{-3}$), therefore, measured resistance change of the SE is conditioned by Joule heating. The values of τ_h measured for 5 CRS lies in the range 20-23 ms. These values are roughly 25% shorter than heat relaxation times reported earlier in the interim report [4].

Making use of the experimentally measured value of τ_h the average heating of the sensor can be estimated from (11) when a sequence of microwave pulses is applied to the RS. Assuming that P=1 kW, τ_h=25 ms, $\tau=10^{-6}$ s, $1/\tau_0$=100 Hz, V=1 mm^3 and taking the values of parameters $d=2.33\cdot10^3$ kg/m^3 and c=760 J/kg/K corresponding to Si at room temperature one can get that the average temperature change is of the order of 1.4 K.

6 Conclusions

- A new concept of the resistive sensor design is proposed. The sensing element is matched with the transmission line and, therefore, it simultaneously serves as a matched load and microwave pulse power sensor.
- The designed and fabricated CRS can measure 1 kW microwave pulses in a wide frequency range with sufficiently small variation of the output signal with frequency.
- Hybrid type filter where the first element of it is partly replaced by the section of conductor coated by the layer of ferrite provides measurements of the microwave pulses in the frequency range 2-12 GHz. The shortest pulse can be measured by this device is roughly 20 ns. To measure shorter pulses the frequency range should be confined. In the frequency range <6 GHz lumped element filter, while in the frequency range 4-12 GHz microstrip filter should be used.
- Designed, fabricated and tested CRS in general meets the requirements of the desirable technical specification. The investigation performed under this contract strongly confirms that the resistive sensors are most perspective devices for HPM pulse measurement.
- The investigation performed within the year revealed what additional investigations should be done to provide HPM source usurers with a new wide frequency range tool for HPM pulse control: (i) the testing of the sensor in a whole frequency range under working conditions, (ii) investigation of the dependence of readings of the CRS on the ambient temperature, (iii) Investigate other possible solutions of the CRS design, (iv) finalizing the selection of the specifications of the CRS with possible users of a new device.

7 References

[1] "Fundamentals of RF and microwave measurements," Application Note 64-1a, Hewlett Packard.

[2] M. Dagys, Ž. Kancleris, R. Simniškis, E. Schamiloglu, F.J. Agee, "Resistive sensor: device for high-power microwave pulse measurement", *IEEE Antennas & Propagation Magazine*, vol. 43, No 5, p. 64-79, 2001.

[3] M. Dagys, Ž. Kancleris, R. Simniškis, E. Schamiloglu, F.J. Agee, X-band resistive sensor for short high-power microwave measurement", *29th European Microwave Conference, Conference Proceedings, Munich, Germany,* October 4-8, 1999, vol. 2, pp.65-68.

[4] "Coaxial-type Resistive Sensor for HPM Applications", Interim report, Microwave Laboratory, Semiconductor Physics Institute, Vilnius, 2002.

[5] V. F. Fusco, Microwave Circuits: Analysis and Computer-aided Design, Prentice-Hall International, 1987.

[6] Kane S. Yee, "Numerical solution of initial boundary problems involving Maxwell's equation in isotropic media", *IEEE Trans. Antennas Propagation*, vol. 14, No 3, p. 302-307, 1966.

[7] Y. Chen, R. Mitra, and P. Harms, "Finite different time domain algorithm for solving Maxwell's equation in rotationally symmetric geometries", *IEEE Trans. Microwave Theory Tech.*, vol. 44, No 6, p.832-838, 1996.

[8] N. Dib, T.Weller, M. Scardelletti, and M. Imparato, "Analysis of cylindrical transmission lines with the finite-difference time-domain method", *IEEE Trans. Microwave Theory Tech.*, vol. 47, No 4, p.509-512, 1999.

8 Acknowledgements

The material presented in this report is based upon work supported by the European Office of Aerospace Research and Development, Air Force Office of Scientific Research, Air Force Research Laboratory under Contract No. F61775-02-WE030. Any opinions, findings and conclusions or recommendations expressed in this material are those of the authors and do not necessarily reflect the views of the European Office of Aerospace Research and Development, Air Force Office of Scientific Research, Air Force Research Laboratory.

The Contractor, Semiconductor Physics Institute, hereby declares that, to the best of its knowledge and belief, the technical data delivered herewith under Contract No. F61775-02-WE030 is complete, accurate and complies with all requirements of the contract.

2003-05-05 Mindaugas Dagys, Dr., Deputy Director of SPI

Disclosures of all subject inventions as defined in FAR 52.227-13 have been reported in accordance with this clause.

2003-05-05 Mindaugas Dagys, Dr., Deputy Director of SPI

9 Appendixes

9.1. Desirable Technical Specifications

The desirable specifications of the coaxial-type RS that we would like to achieve together with the characteristics of a conventional detector are collected in Table 3.

Table 3 Technical characteristics of the proposed coaxial-type RS

	Proposed coaxial-type RS	Conventional detector HP8471E
Frequency range	2 - 10 GHz	0.01 – 12 GHz
Max pulse power	1 kW	200 mW
Flatness of frequency response	±20%`	±0.85 dB
VSRW	<1.6	< 1.2 to 4 GHz < 1.7 to 8 GHz < 2.3 to 12 GHz
Max output signal using 50 V DC pulse supply	~ 7 V	200 mV at $R_L = 50\ \Omega$

9.2. Short description of the FDTD program

The modeled section of the coaxial line with the semiconductor obstacle is shown in **Figure 15**. In the plane $z=z_{ex}$ the regular wave propagating in the coaxial line is excited. It propagates into both sides from the excitation plane. At a distance approximately corresponding to the wavelength of electromagnetic wave in the coaxial line the semiconductor obstacle is placed. In the both ends of the modeled structure absorbing boundary conditions are satisfied. Therefore, the wave propagating left from the excitation plane as well as the wave reflected from the obstacle are absorbed in the plane $z=0$ whereas the wave passed through the obstacle is absorbed int the plane $z=z_{max}$. Determining the components of the electromagnetic field in every point of the line the averaged electric field in the semiconductor obstacle as well as the reflection coefficient from it can be evaluated.

Although the excited wave in the coaxial line has only E_r and H_φ components, in the vicinity of the semiconductor obstacle all components of electromagnetic field can be excited.

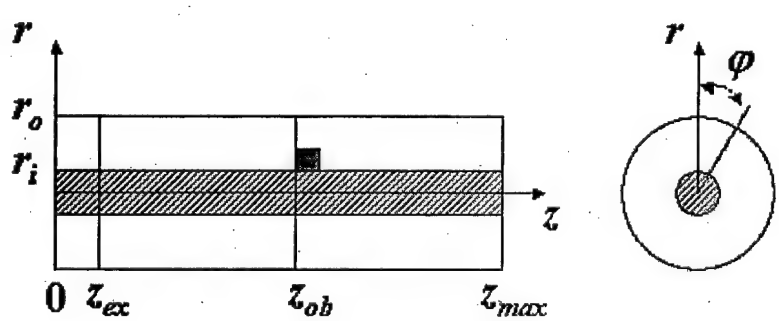

Figure 15. The model of the coaxial line with semiconductor obstacle used for calculations.

Therefore, to determine electric field in the obstacle the Maxwell equations has to be solved and all components of electromagnetic field have to be determined. Introducing dimensionless coordinates r/r_0, z/r_0 and time $t \cdot v/r_0$ where v is a speed of electromagnetic wave in the coaxial line and measuring magnetic field in electric field units $Z_B H$ where Z_B the impedance of free space filled with the same material as the coaxial line, the Maxwell equations in the semiconductor obstacle can be written down in the following way

$$\frac{\partial \mathbf{E}}{\partial t} = (\nabla \times \mathbf{H} - \gamma \mathbf{E}) \frac{\varepsilon}{\varepsilon_c}, \tag{12}$$

$$\frac{\partial \mathbf{H}}{\partial t} = -(\nabla \times \mathbf{E}). \tag{13}$$

Here ε, ε_c are the relative dielectric constant of the semiconductor obstacle and the coaxial line, respectively $\gamma = Z_B r_0 / \rho$, where ρ is the specific resistance of the semiconductor obstacle. In (13) it is assumed that the relative magnetic constant of the coaxial line and semiconductor obstacle is 1. Taking it into account the speed of electromagnetic wave in the coaxial line and impedance of free space filled with the same material as the coaxial line can be expressed in the following way

$$v = \frac{1}{\sqrt{\varepsilon \varepsilon_0 \mu_0}}, \tag{14}$$

$$Z_B = \sqrt{\frac{\mu_0}{\varepsilon \varepsilon_0}}, \tag{15}$$

where ε_0, μ_0 are permittivity and permeability of free space, respectively. Propagation of the wave outside the obstacle is described also by equations (12) and (13) with $\gamma = 0$ and $\varepsilon = \varepsilon_c$.

Equations (12) and (13) have been solved numerically using FDTD (finite difference time domain) method. Therefore, at the first step they should be expanded in cylindrical coordinates, leading to six equations, which relate three components of vector $\mathbf{E}(E_r, E_\varphi, E_z)$ and three components of vector $\mathbf{H}(H_r, H_\varphi, H_z)$. The mesh points where the components of electromagnetic field are calculated are shifted by a half of step [6]-[8]. The elementary cell of the conventional 3-D FDTD lattice in cylindrical coordinates can be chosen in the way shown in **Figure 16**. It is seen that in the elementary cell there are four points located on the middle of the each edge where electric field components are calculated, whereas magnetic field components are computed in the two points that are located in the middle of the surfaces that comprise the elementary cell. Choosing elementary cell in such a way the boundary conditions at any direction has to be satisfied by corresponding electric field components whereas the magnetic field component laying on the boundary surface is calculated using from the boundary condition already determined four electric field component values. It should be mentioned that electric and magnetic field components are determined at different time moments, therefore

$$\begin{aligned} H_r &\Rightarrow H_{r_{(i,j+\frac{1}{2},k+\frac{1}{2})}}^{(n+1/2)} & E_r &\Rightarrow E_{r_{(i+\frac{1}{2},j,k)}}^{(n)} \\ H_\varphi &\Rightarrow H_{\varphi_{(i+\frac{1}{2},j,k+\frac{1}{2})}}^{(n+1/2)} & E_\varphi &\Rightarrow E_{\varphi_{(i,j+\frac{1}{2},k)}}^{(n)} \\ H_z &\Rightarrow H_{z_{(i+\frac{1}{2},j+\frac{1}{2},k)}}^{(n+1/2)} & E_z &\Rightarrow E_{z_{(i,j,k+\frac{1}{2})}}^{(n)} \end{aligned} . \tag{16}$$

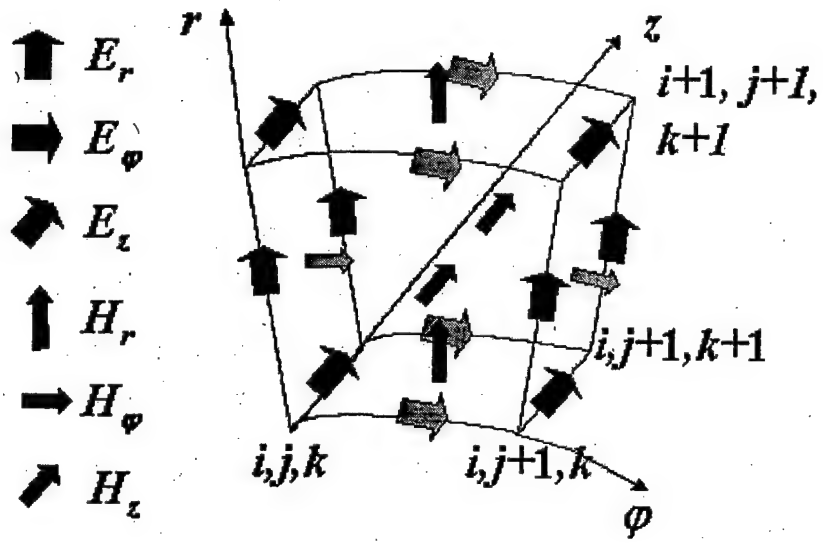

Figure 16. An elementary 3-D FDTD cell in cylindrical coordinate system. The arrows denote the points where particular component of electromagnetic field is calculated.

In these expressions the upper index corresponds to the number of the time step, while the lower – to the number of coordinate step: $i \Rightarrow r$, $j \Rightarrow \varphi$, and $k \Rightarrow z$. By discretizing time and coordinate derivatives in (12) and (13) one will arrive to the following expressions:

$$H_{r_{(i,j+\frac{1}{2},k+\frac{1}{2})}}^{(n+1/2)} = H_{r_{(i,j+\frac{1}{2},k+\frac{1}{2})}}^{(n-1/2)} + \frac{\Delta t}{\Delta z}\left[E_{\varphi_{(i,j+\frac{1}{2},k+1)}}^{(n)} - E_{\varphi_{(i,j+\frac{1}{2},k)}}^{(n)}\right] - \frac{\Delta t}{\Delta\varphi(r_i + i\Delta r)}\left[E_{z_{(i,j+1,k+\frac{1}{2})}}^{(n)} - E_{z_{(i,j,k+\frac{1}{2})}}^{(n)}\right]$$

$$H_{\varphi_{(i+\frac{1}{2},j,k+\frac{1}{2})}}^{(n+1/2)} = H_{\varphi_{(i+\frac{1}{2},j,k+\frac{1}{2})}}^{(n-1/2)} + \frac{\Delta t}{\Delta r}\left[E_{z_{(i+1,j,k+\frac{1}{2})}}^{(n)} - E_{z_{(i,j,k+\frac{1}{2})}}^{(n)}\right] - \frac{\Delta t}{\Delta z}\left[E_{r_{(i+\frac{1}{2},j,k+1)}}^{(n)} - E_{r_{(i+\frac{1}{2},j,k+1)}}^{(n)}\right]$$

$$\begin{aligned} H_{z_{(i+\frac{1}{2},j+\frac{1}{2},k)}}^{(n+1/2)} &= H_{z_{(i+\frac{1}{2},j+\frac{1}{2},k)}}^{(n+1/2)} + \frac{\Delta t}{\Delta\varphi(r_i + (i+1/2)\Delta r)}\left[E_{r_{(i+\frac{1}{2},j+1,k)}}^{(n)} - E_{r_{(i+\frac{1}{2},j,k)}}^{(n)}\right] \\ &- \frac{\Delta t}{\Delta r}\left[E_{\varphi_{(i+1,j+\frac{1}{2},k)}}^{(n)} - E_{\varphi_{(i,j+\frac{1}{2},k)}}^{(n)}\right] - \frac{\Delta t/2}{\Delta\varphi(r_i + (i+1/2)\Delta r)}\left[E_{\varphi_{(i+1,j+\frac{1}{2},k)}}^{(n)} + E_{\varphi_{(i,j+\frac{1}{2},k)}}^{(n)}\right] \end{aligned} \tag{17}$$

$$E_{r_{(i+\frac{1}{2},j,k)}}^{(n+1)} = E_{r_{(i+\frac{1}{2},j,k)}}^{(n)}\left(1-\frac{\Delta t\gamma\varepsilon}{\varepsilon_c}\right)+\frac{\Delta t\varepsilon}{\Delta\varphi(r_i+(i+1/2)\Delta r)\varepsilon_c}\left[H_{z_{(i+\frac{1}{2},j+\frac{1}{2},k)}}^{(n+1/2)}-H_{z_{(i+\frac{1}{2},j-\frac{1}{2},k)}}^{(n+1/2)}\right]$$
$$-\frac{\Delta t\varepsilon}{\Delta z\varepsilon_c}\left[H_{\varphi_{(i+\frac{1}{2},j,k+\frac{1}{2})}}^{(n+1/2)}-H_{\varphi_{(i+\frac{1}{2},j,k-\frac{1}{2})}}^{(n+1/2)}\right]$$

$$E_{\varphi_{(i,j+\frac{1}{2},k)}}^{(n+1)} = E_{\varphi_{(i,j+\frac{1}{2},k)}}^{(n)}\left(1-\frac{\Delta t\gamma\varepsilon}{\varepsilon_c}\right)+\frac{\Delta t\varepsilon}{\Delta z\varepsilon_c}\left[H_{r_{(i,j+\frac{1}{2},k+\frac{1}{2})}}^{(n+1/2)}-H_{r_{(i,j+\frac{1}{2},k-\frac{1}{2})}}^{(n+1/2)}\right]$$
$$-\frac{\Delta t\varepsilon}{\Delta r\varepsilon_c}\left[H_{z_{(i+\frac{1}{2},j+\frac{1}{2},k)}}^{(n+1/2)}-H_{z_{(i-\frac{1}{2},j-\frac{1}{2},k)}}^{(n+1/2)}\right] \tag{18}$$

$$E_{z_{(i,j,k+\frac{1}{2})}}^{(n+1)} = E_{z_{(i,j,k+\frac{1}{2})}}^{(n)}\left(1-\frac{\Delta t\gamma\varepsilon}{\varepsilon_c}\right)-\frac{\Delta t\varepsilon}{\Delta\varphi(r_i+i\Delta r)\varepsilon_c}\left[H_{r_{(i,j+\frac{1}{2},k+\frac{1}{2})}}^{(n+1/2)}-H_{r_{(i,j-\frac{1}{2},k+\frac{1}{2})}}^{(n+1/2)}\right]$$
$$+\frac{\Delta t\varepsilon}{\Delta r\varepsilon_c}\left[H_{\varphi_{(i+\frac{1}{2},j,k+\frac{1}{2})}}^{(n+1/2)}-H_{\varphi_{(i-\frac{1}{2},j,k+\frac{1}{2})}}^{(n+1/2)}\right]+\frac{\varepsilon\Delta t/2}{(r_i+i\Delta r)\varepsilon_c}\left[H_{\varphi_{(i+\frac{1}{2},j,k+\frac{1}{2})}}^{(n+1/2)}+H_{\varphi_{(i-\frac{1}{2},j,k+\frac{1}{2})}}^{(n+1/2)}\right]$$

As follows from (17) and (18) in the first time step the new values of magnetic field components are evaluated using previous values of components calculated earlier, while in the next step the values of magnetic field components are used to update electric field components values. As it was already mentioned outside the semiconductor obstacle $\gamma = 0$ and $\varepsilon = \varepsilon_c$.

Making use (17) and (18) electric and magnetic field components can be calculated at any point of the modeled structure at any time moment. Regular varying in time electric field component E_r is added to the calculated value in the plane $z=z_{ex}$ providing two regular waves propagating to right and left sides from the excitation plane. To get a solution the problem initial and boundary condition has to be formulated. At $t = 0$ there is no any electric or magnetic field in the coaxial line, therefore, all components of electric and magnetic field should be zero. When the dimensions of the semiconductor obstacle is much less than the characteristic dimensions of the coaxial line the stationary solution is obtained faster when the regular initial wave is inserted into modeled structure.

As it was already mentioned the boundary conditions using chosen elementary 3D FDTD cell **Figure 16** should be formulated for the corresponding components of the electric field only. As can be easily seen from the figure the components E_φ and E_r should satisfy non-reflecting boundary conditions in the planes $z = 0$ and $z = z_{\max}$. On the inner and outer conductors the electric field components laying in the conductor surfaces should be zero:

$$\begin{aligned} &E_\varphi(r_i,\varphi,z)=0, \quad E_\varphi(r_o,\varphi,z)=0,\\ &E_z(r_i,\varphi,z)=0, \quad E_z(r_o,\varphi,z)=0. \end{aligned} \tag{19}$$

Semiconductor obstacle is placed either on the inner or the outer conductors of the coaxial line. When the height of the obstacle is less than the span between conductors it was assumed that in the surface that limits the obstacle in r direction electric field components E_φ and E_r should be zero. In this way the upper metal contact is accounted in the calculations.

When choosing step size the Courant criterion that defines the ratio between time and coordinate steps has to be taken into account [6]. Calculated electric and magnetic field strengths were normalized to the electric field strength on the inner conductor $E_r(r_i, \varphi, z)$ in the empty coaxial line, therefore, normalization constant can be expressed as follows

$$E_{norm} = 84.796\sqrt{\frac{P}{\varepsilon Z_C}}\frac{1}{r_i}, \tag{20}$$

where P is power propagating in the coaxial line, Z_C is the impedance of coaxial line and r_i is the radius of inner conductor.

Since the coaxial line with the obstacle has a symmetry plane $r0z$ lying in the center of the obstacle, only half of the plane in φ direction has been modeled. The squares of electromagnetic field components calculated at each point of the modeled structure is summed and stored in additional arrays. After each period the amplitudes of E_r calculated in the plain $r0z$ lying in the center of the obstacle were compared with the values calculated one period earlier. If the largest difference between these values was less than the predetermined value δ the calculations have been finished otherwise the successive period has been modeled. When the size of the semiconductor obstacle is sufficiently small 5% accuracy is achieved within two or three periods.

The program calculating the components of the electromagnetic field in the coaxial line with semiconductor obstacle has been written using C programming language. Calculations have been performed using personal computer AMD XP 1600+ with 512 MB RAM. Having about 10^6 points for each component and modeling 500 steps per period it takes about 1.5 h to get the solution.

A few tests of the program have been performed. In the first one the parameters of the obstacle has been set to be equal to the parameters of the material that fills the coaxial line ($\varepsilon = \varepsilon_c = 1$ and $1/\rho = 0$). Therefore, in the line we should have only E_r and H_φ components of the electromagnetic field the amplitudes of which should correspond to the stationary distribution in the coaxial line. Taking into account that the amplitudes of the electric and magnetic fields are normalized to its value on the surface on the inner conductor at the grid points they can be expressed as follows

$$\frac{E_r(i)}{E_r(r_i)} = \frac{H_\varphi(i)}{H_\varphi(r_i)} = \frac{r_i}{r_i + (i - 0.5)\cdot\Delta r}, \tag{21}$$

where $i = 1, 2, ..., i_{\max} - 1$, and $i_{\max}$ is maximum number of points in the grid in **r** direction. Calculated distributions of E_r and H_φ in z direction in the grid $i_{\max} \times j_{\max} \times k_{\max} = 17 \times 52 \times 240$ for different i are shown in **Figure 17** by solid lines. The dashed lines present the values calculated using (21). It is seen that the reflection from both ends of the coaxial line is negligible and after 4 periods of calculation obtained distribution of electric and magnetic field components exactly corresponds to the values calculated from (21).

In the other test we compared the values of reflection coefficient from the semiconductor obstacle in the coaxial line calculated using FDTD program and in the impedance approximation. The model of the obstacle that partly fills the coaxial line is shown in **Figure 18**. The parameters of the obstacle and the coaxial line were the following: $\varphi_o = 67.5°$, $r_i = 2$ mm, $r_o = 4.6$ mm, h=2.6 mm and the length of the obstacle in z direction l=1.58 mm. Relative dielectric constant of the obstacle ε=11.9 corresponds to the dielectric

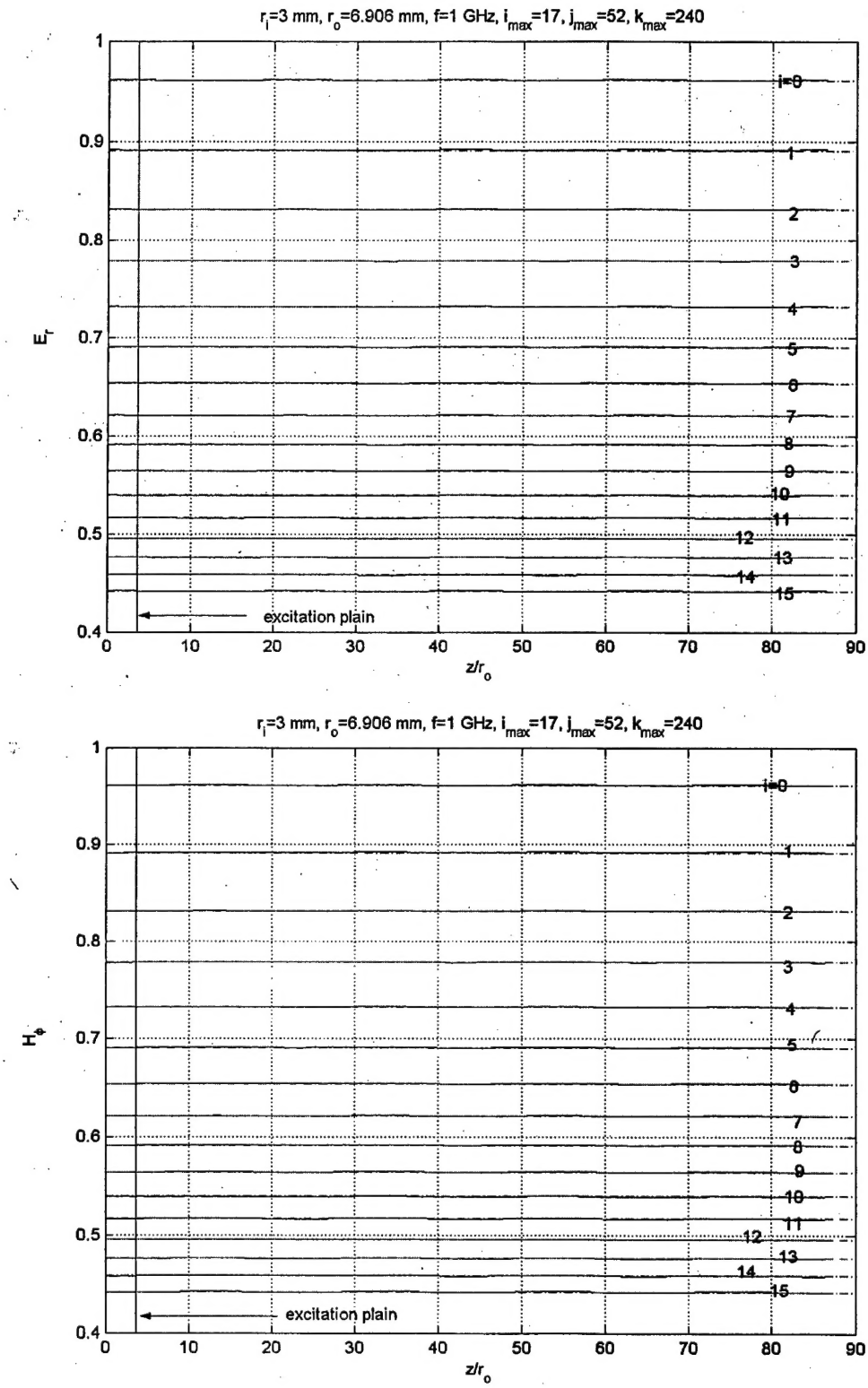

Figure 17. Calculated distribution of E_r (upper graph) and H_φ (lower graph) in the empty coaxial line (solid lines) and exact values calculate according to (21) (dashed lines) in different layers after four periods of calculation.

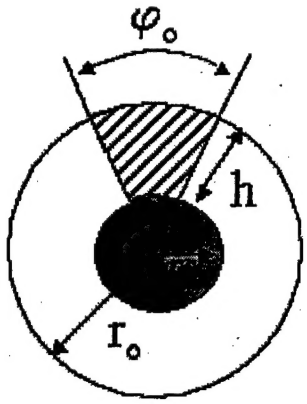

Figure 18. The model of the semiconductor obstacle in the coaxial line.

constant of Si. The reflection coefficient of the obstacle can be determined using well-known formula

$$\Gamma_E = \frac{Z_O - Z_C}{Z_O + Z_C}, \qquad (22)$$

where Z_O is the impedance of the obstacle, and Z_C is the impedance of the coaxial line. When determining Z_O the resistance and capacitance of the obstacle as well as the impedance of the coaxial line behind the obstacle is taken into account.

Calculated reflection coefficient dependences on specific resistance of the obstacle for different frequencies are presented in **Figure 19**. Reflection coefficient values calculated using FDTD program are shown by points, whereas solids lines present the results obtained in impedance approximation using expression (22). As it might be expected good coincidence between obtained results is observed in the low frequency region where the characteristic dimensions of the obstacle is much smaller than the wavelength of the microwave. When the frequency increases the coincidence between two approximations becomes worse. It is seen that at a frequency of 10 GHz dependences differ even qualitatively predicting different dependence of the reflection coefficient on specific resistance of the obstacle.

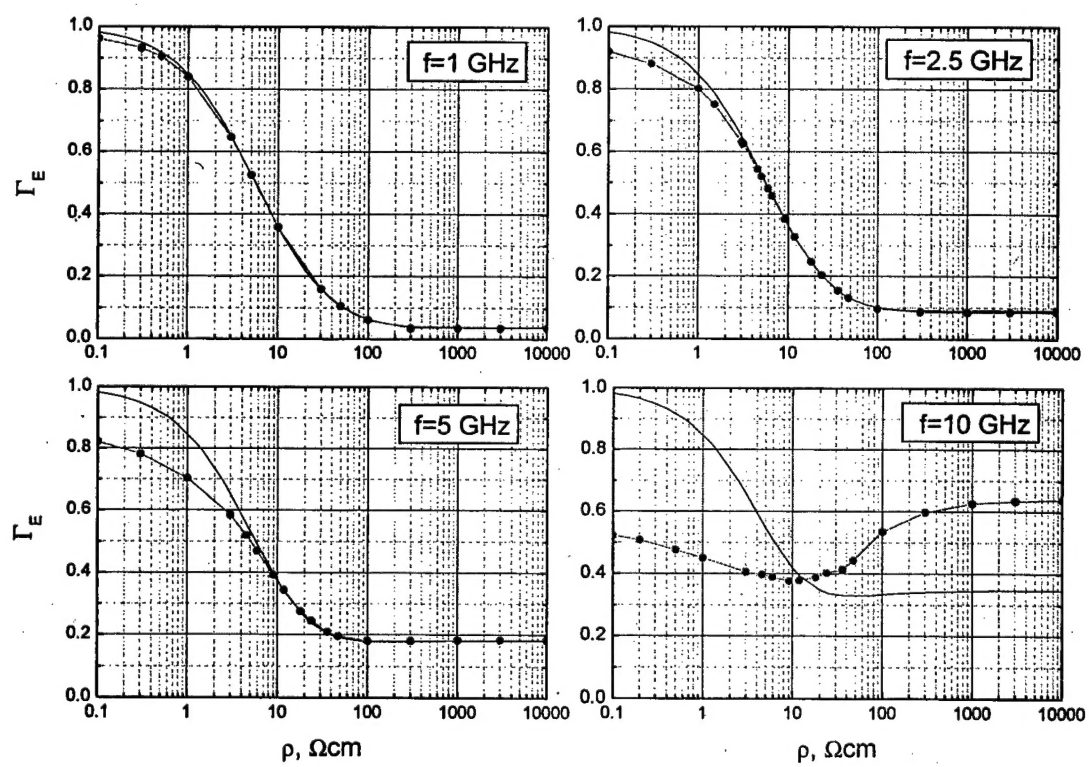

Figure 19. The dependences of the reflection coefficient on the specific resistance of the semiconductor obstacle that partly fills the coaxial line at different frequencies. Solid line demonstrates impedance approximation; points are calculated using FDTD method.

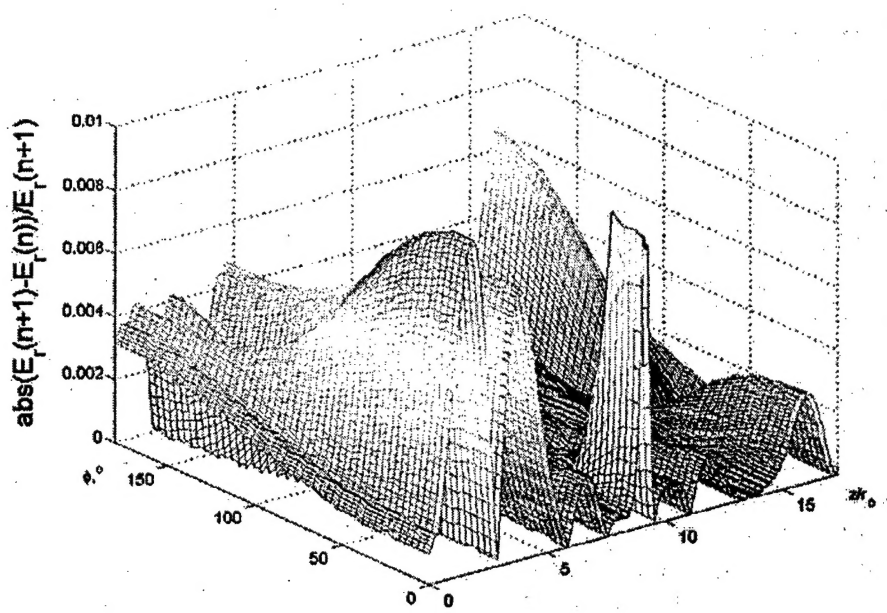

Figure 20. Relative absolute difference between the amplitudes of E_r computed at third and at second periods of the calculation in the $\varphi 0z$ plane closest to the inner conductor of the coaxial line. Calculation parameters: f=5 GHz, r_i=3 mm, r_o=6.9 mm. Parameters of obstacle: h=3 mm, φ_0=28.2 °, l=1.5 mm, ρ=30 Ωcm obstacle is placed on the inner conductor of the coaxial line.

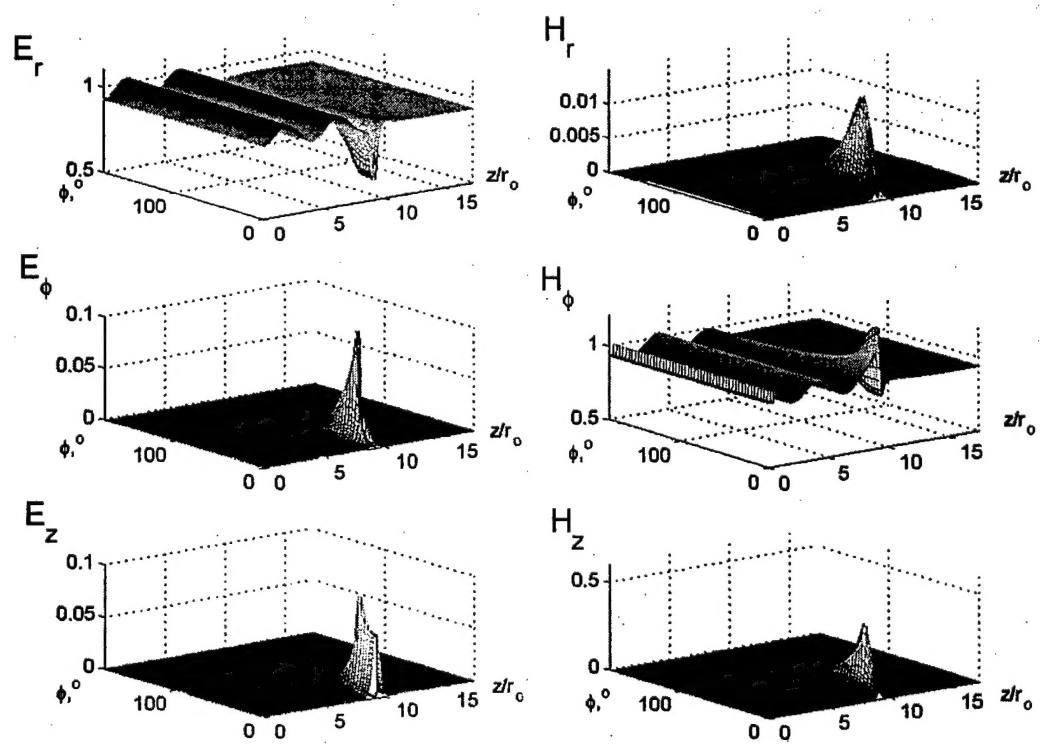

Figure 21. The distribution of the amplitudes of electric and magnetic field components in the $\varphi 0z$ plane closest to the inner conductor of the coaxial line. Calculation parameters and the size of the obstacle are the same as in **Figure 20**.

Typical calculation accuracy that can be achieved using our program illustrates data presented in **Figure 20**, where the distribution in $\varphi 0z$ plane of the relative absolute difference between the amplitudes of E_r calculated during the last period of the modeling and one period before is shown. As it was already mentioned we have modeled only half of the plane in φ direction. The number of points in each direction was the following: $r \rightarrow 17$, $\varphi \rightarrow 52$, $z \rightarrow 480$. Obstacle was placed on the inner conductor and has been modeled making use 13, 6, 7 points in corresponding direction, respectively. Although the height of the obstacle is only slightly less then the span between inner and outer conductors, as follows from the figure, good calculation accuracy is achieved after three periods of modeling.

Calculated distribution of the electromagnetic field components for this particular calculation is shown in **Figure 21**. It is seen that in the obstacle the amplitude of the regular components of the electric field E_r decreases whereas the amplitude of the magnetic field H_φ increases. In the close proximity to the obstacle the standing modes of the other components of the electric and magnetic field are excited. Due to reflection from the semi-conducting obstacle partly standing wave is formed before it (VSWR=1.13). It also should be mentioned that we succeeded to formulate perfect non-reflecting boundary conditions for the ends of the coaxial line with reflection coefficient of the order of 10^{-3}. The averaged values of the components of electric and magnetic field in the obstacle were the following: $\langle E_r \rangle$=0.418, $\langle E_\varphi \rangle$=0.014, $\langle E_z \rangle$=0.013, $\langle H_r \rangle$=0.004, $\langle H_\varphi \rangle$=0.731 and $\langle H_z \rangle$=0.148. It is worth to remind that the amplitude of the electric field is normalized to the amplitude of the E_r on the surface of the inner conductor in the empty coaxial line and the magnetic field components are measured in the same units as electric field. As follows from the presented data only small average amplitude of electric field components E_φ and E_z is induced in the obstacle, roughly 3% of the regular component E_r. The amplitude of H_z was up to 20 % of H_φ.

The tests performed with the written FDTD program have proved its suitability and we were able to use it for the calculation of the electromagnetic field components in the semiconductor obstacle placed in the coaxial line.